Hierarchical porous nano-carbon composite: Effective fabrication and application in dye sensitized solar cells

Wei Zeng [a,b], Guojia Fang [a,*], Xueqi Wang [a], Qiao Zheng [a], Borui Li [a], Huihui Huang [a], Hong Tao [a], Nishuang Liu [a], Weijun Xie [b], Xingzhong Zhao [a], Dechun Zou [c]

[a] Key Laboratory of Artificial Micro- and Nano-structures of Ministry of Education of China, Department of Electronic Science and Technology, School of Physics and Technology, Wuhan University, Wuhan 430072, PR China
[b] College of Science, Jiujiang University, Jiujiang 332005, PR China
[c] Beijing National Laboratory for Molecular Sciences, Key Laboratory of Polymer, Chemistry and Physics of Ministry of Education, College of Chemistry and Molecular Engineering, Peking University, Beijing 100871, PR China

HIGHLIGHTS

► The dye sensitized solar cell owns relatively high efficiency.
► The fabrication method is greatly effective and low-cost.
► A facile pore-forming precursor is employed.
► The counter electrode owns unique hierarchical porous structure.
► A theoretical simulation convincingly demonstrates the experimental results.

GRAPHICAL ABSTRACT
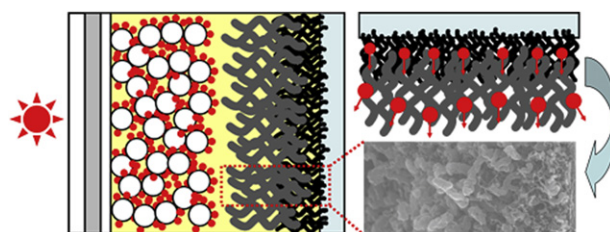
ABSTRACT

A nano-carbon composite with unique hierarchical porous structure has been effectively fabricated as dye sensitized solar cell (DSSC) counter electrode material by a simple and low-cost way. The fabrication process only employs spin-coating and then combustion by using sodium lauryl sulfate as a facile pore-forming precursor. The generated composite reveals high catalytic ability coupled with low electrical resistance owing to its unique structure. The power conversion efficiency of the resulting DSSC device reaches 6.5%, which is close to 6.6% of the referenced DSSC by using platinum as the counter electrode. A mass transfer model is built and it convincingly demonstrates that the composite architecture is beneficial to carrier transport. The fabrication strategy is simple and effective, and it has a great potential to be applied to DSSC fabrication on a large scale.

© 2012 Elsevier B.V. All rights reserved.

1. Introduction

To date, the dye sensitized solar cells (DSSCs) have attracted more and more attention for its advantages of low production costs and high energy-conversion efficiencies, especially when an efficiency record of 12% was established recently [1–4]. A typical DSSC has a sandwich-like structure including illuminated photoanode, counter electrode (CE) and redox electrolyte. A general CE is a fluorine-doped tin oxide (FTO) conducting glass coated by platinum (Pt) film. As a nobler metal, Pt is expensive even though it brings high catalytic ability [1,2]. Hence, a number of low-cost alternatives with high catalytic ability have been explored,

including carbon-based materials, polyaniline, poly (3,4-ethylene dioxythiophene) and their combinations [5–15].

Due to its large surface area, one-dimensional carbon nanomaterial (OCN), such as carbon nanotubes (CNTs) and nanofibers (CNFs), reveals admirable catalysis activity for DSSC CE [7–10]. The highest efficiency of 10% is obtained based on a CE with an aligned carbon nanotubes [10]. However, its fabrication employs a complex chemical vapor deposition system. The flame synthesis is relatively simple and low cost, and it has been widely applied to fabricate OCN [16–18]. The generated OCN reveals good electrical connectivity, which is similar to aligned carbon nanotubes. However, its catalytic ability is not high enough. For enhancement of the catalytic ability, the conventional way is to increase the quantity of OCN by increasing the quantity of its inductor in fabrication process [7]. However, the inductor's quantity is restricted. Only the inductor in nanoscale range can validly induce OCN's growth, and the excess will make the OCN yield to decrease. In addition, there is another way to enhance the catalytic ability by enlarging of the surface area of ready-made OCN. It is operated by dispersing the original OCN in solution and then recoating it on substrate [19,20]. However, this method is very complex.

In this paper, a simple and effective method is developed to enhance the OCN's catalytic ability. The fabrication process only employs spin-coating and then combustion in ethanol flame by using a facile pore-forming precursor of sodium lauryl sulfate ($C_{12}H_{25}NaO_4S$, K12). The generated CNTs and CNFs composite (CNNC) owns unique hierarchical porous structure, results in the high catalytic ability coupled with low electrical resistance. The power conversion efficiency of the resulting DSSC device reaches 6.5%, which is close to 6.6% of the referenced DSSC by using Pt-based CE. Systematic characterizations are presented and a mass transport model is built. The simulation results demonstrate that the composite structure is beneficial to carrier transport. The procedure is simple and effective, and it has a great potential to be applied to DSSC fabrication on a large scale.

2. Experimental details

2.1. Materials

Ti foil (purity 99.7%), tetrabutyl titanate, diethanol amine, ethanol, hydrochloric acid, nitric acid, glacial acetic acid, polyethylene glycol, acetonitrile, propylene carbonate (PC), nickel sulfate hexahydrate ($NiSO_4 \cdot 6H_2O$, $NiSO_4$) and K12 were obtained from Sinopharm Chemical Reagent Corporation (China). PMII (1-methyl-3-propyl imidazolium iodide), Iodine (I_2, AR), 4-tert-butylpyridine (TBP) and guanidine thiocyanate (GuSCN) were purchased from Aladdin-reagent. The Ru dye (cis-di(thiocyanato))-N-N′-bis(2,2′-bipyridyl-4-carboxylic acid-4-tetrabutylammonium carboxylate) ruthenium (II) (N719), was purchased from Solaronix (Switzerland). Lithium iodide (LiI, 99.99%) and titanium isopropoxide were obtained from Acros. All the reagents not indicated were of analytical purity. FTO glass with sheet resistance about 14 Ω sq^{-1} and indium tin oxide (ITO) glass with sheet resistance about 8 Ω sq^{-1}, were purchased from Asahi Glass (Japan).

2.2. Preparation and measurement of CEs

The as-prepared cell is illustrated in Fig. 1 with the hierarchical CNNC as CE. The Ti substrates were firstly polished with graded roughness abrasive papers and then rinsed with detergent and deionized water. Next, the substrates were soaked in dilute hydrochloric acid for 30 min, and then be sonicated 10 min in ethanol and 10 min in acetone.
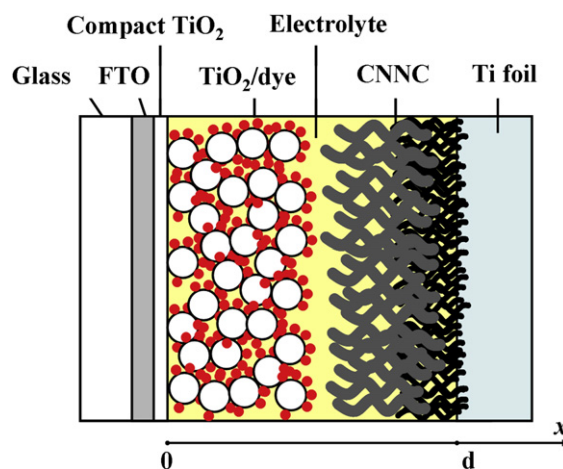

Fig. 1. Schematic of the DSSC with the hierarchical porous CNNC CE.

Aqueous solution including different content of $NiSO_4$ and K12 were prepared in 70 °C. Then, a layer of solution was spin-coated on a Ti foil. After inartificial dried in air for 30 min, the coated foil was moved into an ethanol flame for 5 min. The detailed flame synthesis method can refer to the literature [16]. The referenced Pt CE was fabricated by sputtering a thin layer of Pt on ITO substrate.

The weight of each CNNC CE was measured before the solution was coated and after the substrate was combusted, and denoted as m_0 and m_1, respectively. Then, the weight of the generated CNNC is obtained by $m_1 - m_0$. The surface area of substrate is $m_0/\rho_{substrate}/d_{substrate}$, where the $\rho_{substrate}$ means the density of Ti material set as 4.5 g cm^{-3}, and the $d_{substrate}$ is the thickness of the substrate, measured as 0.02 cm. Then, the weight of CNNC per square centimeter (m_{CNNC}) is $(m_1 - m_0)/(m_0/\rho_{substrate}/d_{substrate})$.

2.3. Preparation of photoanodes

The photoanodes were prepared according to the literature [5,21,22]. A compact TiO_2 solution and a porous TiO_2 gel were prepared. Firstly, a 50 nm compact TiO_2 film was coated on a clean FTO substrate by spin-coating method and retained at 550 °C for 30 min. Then, a porous TiO_2 film of 14 μm was coated on compact layer by doctor-blade method, subsequently retained at 500 °C for 30 min. After cooled to 120 °C, the substrates were dipped into 0.3 mM N719 ethanol solution and kept at 60 °C for 12 h so as to absorb the dye adequately.

2.4. Characteristics

The morphology of composite CE material was observed by scanning electron microscopy (SEM, JSM 6700F) and high resolution transmission electron microscopy (HRTEM, JEOL JEM 2010).

The photovoltaic characteristics were recorded by a standard ABET Sun 2000 Solar Simulator under 100 mW cm^{-2}, AM 1.5 simulated irradiation. The electrolyte contains 1 M PMII, 0.04 M LiI, 0.03 M I_2, 0.1 M GuSCN and 0.5 M TBP in a solution of acetonitrile and PC (v:v = 1:1). Cyclic voltammetry (CV), Tafel polarization measurement and electrochemical impedance spectroscopy (EIS) were measured with a symmetrical dummy CE–CE cell. The identical CEs were separated by a Teflon film of 100 μm (d_{space}). Photocurrent density–voltage (J–V) characteristics, CV, Tafel and EIS were collected using a CHI 660D electrochemical workstation (ShangHai, China). Irradiated area of the cells was kept as 0.25 cm^2 in J–V measurements. The EIS was performed with the frequency ranging from 100 kHz to 0.1 Hz at zero bias potential. The BET

(Brunauer–Emmett–Teller) surface area and porosity was measured by a static nitrogen adsorption instrument in 77 K (JW-BK, Beijing, China). The Raman spectra were measured with 488 nm laser excitation by a LabRAM HR800.

3. Numerical simulation

3.1. Simulation procedure

The entire DSSC device is simulated by a mass transport model with finite element method refers to the literature [23–25]. In literature, the cell is modeled as a one-dimensional, pseudo-homogeneous medium, which is intermixed by porous TiO_2, dye and electrolyte when the CE is a planar Pt [23]. Yet in this paper the porous CNNC is added in the medium when the CE is switched to porous CNNC. Fig. 1 illustrates the modeled region in the real DSSC device. It is in the range of 0 to d on the x-axis, where $x = 0$ and $x = d$ mean the interfaces of FTO to compact TiO_2, and CNNC layer to the Ti substrate, respectively. The carriers being studied here involve the electrons, iodide I^-, triiodide I_3^- and cation. They are driven by continuity equations and transport equations. The inner macroscopic electric field is calculated by using Poisson's equation. These differential equations and related boundary conditions refer to those in the literature [23].

3.2. The functional parameters for simulation

The functional simulation parameters related to the investigated CE are obtained according to the experiment results in this paper. The porosity was measured by the static nitrogen adsorption instrument. The serial resistance R_S was extracted from the fitting values of Nyquist plots. The length of model medium (d) was calculated by $d = d_{TiO_2} + d_{CNNC}$. Here, d_{TiO_2} and d_{CNNC} are the thicknesses of porous TiO_2 layer on photoanode and CNNC layer on CE, respectively. The diffusion coefficient (D) of I_3^- ($D_{I_3^-}$) was extracted by measuring the limiting current density (J_{lim}) from CV plots with the symmetrical dummy cells. The initial concentration of I_3^- ($n_{I_3^-,0}$) equals to that of I_2. When J_{lim} are measured, $D_{I_3^-}$ can be obtained by $D_{I_3^-} = J_{lim} \cdot d_{CEs}/(4Fn_{I_3^-,0})$, where F is Faraday's constant, d_{CEs} is the distance between two CEs with $d_{CEs} = 2 \times d_{CNNC} + d_{space}$. The diffusion coefficient of I^- is assumed as the same as that of I_3^-.

4. Results and discussion

4.1. J–V characteristics

For investigating the quantity influence of the $NiSO_4$ and K12 on the performance of DSSC device, a series of CEs are fabricated with different $NiSO_4$ and K12 contents. The $J–V$ characteristics are shown in Fig. 2, and related results such as open circuit voltage (V_{OC}), short current density (J_{SC}), fill factor (FF) and power conversion efficiency (PCE), are listed in Table 1. It is clearly illustrated that the content effect is remarkable. With 0.250 M $NiSO_4$ and 2 mM K12 (CE2), the cell achieves a high efficiency of 6.5%, which approaches 6.6% of the referenced Pt-based DSSC (CE0).

4.2. Morphology characteristics of CEs

For study the roles of $NiSO_4$ and K12 on the CE morphology, the CNNC CEs are visualized by SEM on various magnifications. Two typical CEs are shown in Fig. 3. The CE2 gives the cell the highest PCE among these CNNC CEs. Compared to CE2, the CE4 is fabricated with the same $NiSO_4$ content but without K12. As shown in Fig. 3 (a1–3), the CE4 exhibits a homogeneous surface composed of
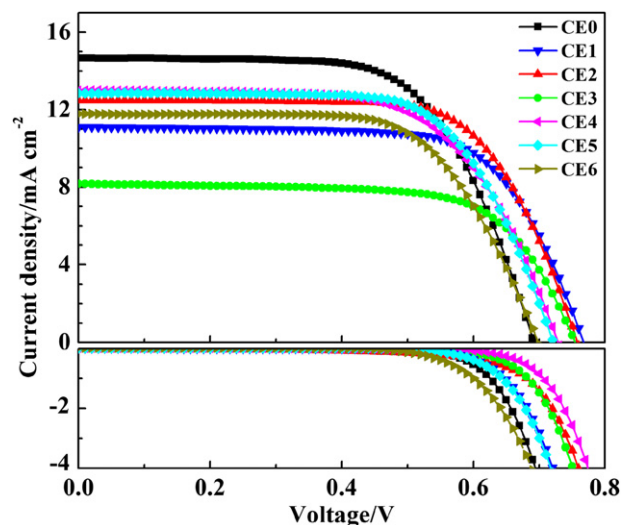

Fig. 2. The photovoltaic J–V curves (upper part) and dark J–V curves (lower part) of DSSCs.

small-size nanostructure. Whereas the CE2 (Fig. 3 (b1–2)) exhibits a ridge-like surface. The under-layer (Fig. 3 (b3.1)) is similar to CE4, yet the top-layer (Fig. 3 (b3.2)) shows relatively bulkier nanostructure. These features are more obvious in cross section views (Fig. 3 (a4) and (b4)), indicating the CE2 prepared with the K12 is hierarchical. This feature is also observed on other CNNC CEs prepared with the K12, as shown in Fig. 4.

In general, the as-generated nanostructure prepared without the K12 is almost compact and even partly block at bottom (Fig. 3 (a4) for CE4). With a small concentration ratio of the K12 to $NiSO_4$, a porous nanostructure is generated with a clear boundary to the compact part (Fig. 4 (b) for CE3, Fig. 3 (b4) for CE2). With the increase of concentration ratio, the forementioned boundary turns unobvious (Fig. 4 (a) for CE1, Fig. 4 (c) for CE5). With the biggest K12 to $NiSO_4$ ratio, almost only porous part is shown (Fig. 4 (d) for CE6). These illustrate the K12 dramatically affects the hierarchical feature.

The relatively compact even block part is named as compact layer, and the relatively porous part is named as porous layer. The two layers are clearly indicated as region A and B, respectively, in related SEM images. The thicknesses of compact ($d_{compact}$) and porous layers (d_{porous}) are measured and the entire nano-carbon thickness (d_{CNNC}) are calculated by $d_{CNNC} = d_{compact} + d_{porous}$, listed in Table 2. For the CE1 and CE5, only d_{CNNC} values are given because of the unclear boundaries as mentioned above. Specifically, in the case of same K12 concentration, the $d_{compact}$ increases and d_{porous} changes slightly with increasing $NiSO_4$ concentration. In the case of same $NiSO_4$ concentration, the d_{porous} increases and $d_{compact}$ almost remain unchanged with increasing K12 concentration.

Table 1
The J–V characteristics of the DSSCs.[a]

CE	$NiSO_4$ (M)	K12 (mM)	V_{OC} (V)	J_{SC} (mA cm^{-2})	FF	PCE (%)
CE0	–	–	0.70 ± 0.02	14.7 ± 0.1	0.64 ± 0.01	6.6 ± 0.3
CE1	0.125	2	0.77 ± 0.03	11.1 ± 0.1	0.69 ± 0.02	5.9 ± 0.3
CE2	0.250	2	0.76 ± 0.03	12.5 ± 0.1	0.69 ± 0.02	6.5 ± 0.4
CE3	0.500	2	0.76 ± 0.03	8.2 ± 0.1	0.68 ± 0.02	4.2 ± 0.3
CE4	0.250	0	0.73 ± 0.03	13.0 ± 0.2	0.63 ± 0.03	6.0 ± 0.5
CE5	0.250	4	0.73 ± 0.03	12.9 ± 0.1	0.66 ± 0.02	6.2 ± 0.4
CE6	0.250	6	0.70 ± 0.03	11.8 ± 0.1	0.65 ± 0.02	5.4 ± 0.3

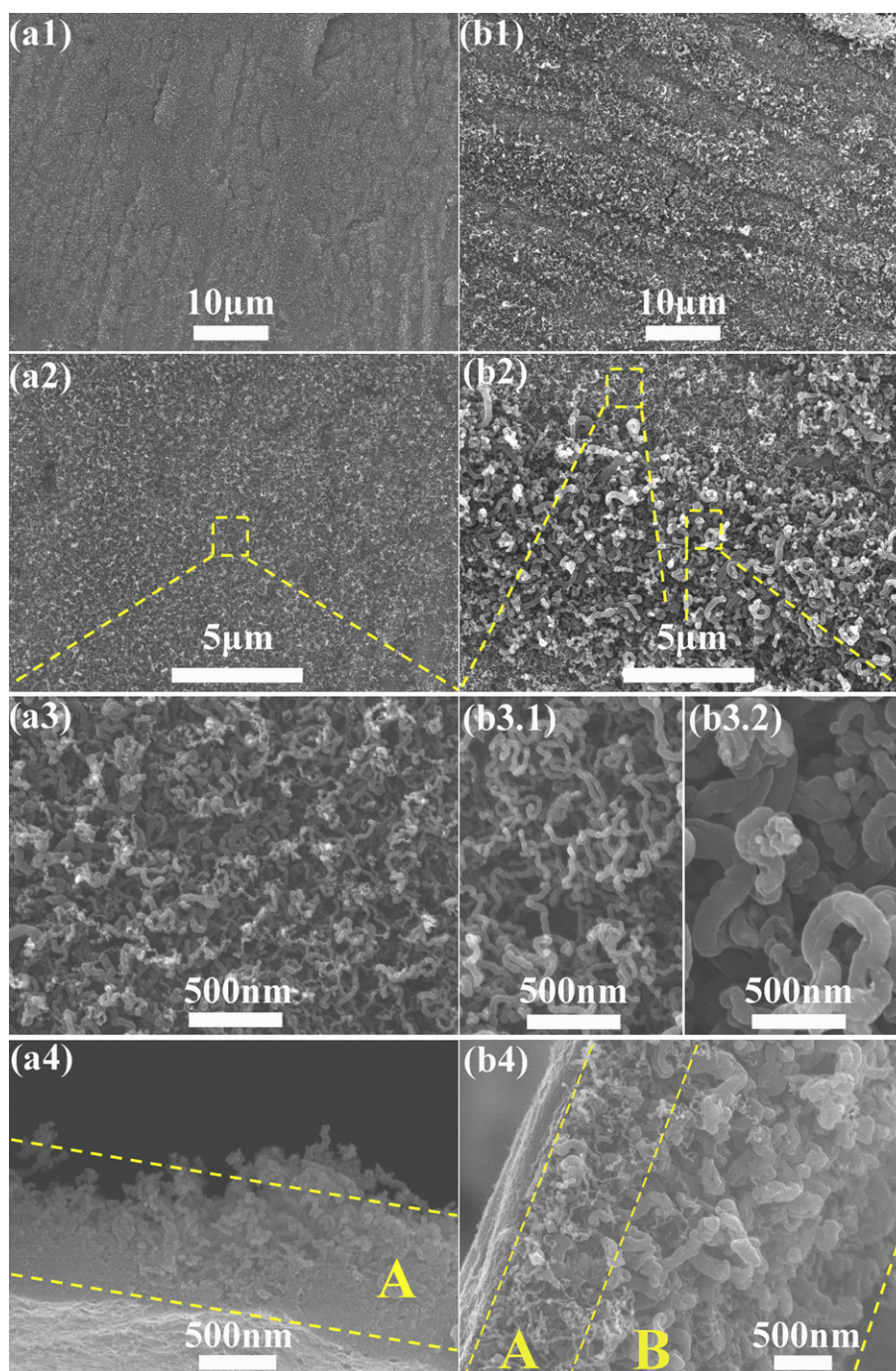[a] The results with standard error are obtained by five samples.

Fig. 3. The SEM images of CE4 and CE2 on various magnifications. CE4: top view (a1, a2, and a3), side view (a4). CE2: top view (b1, b2, b3.1 and b3.2), side view (b4).

These indicate the NiSO$_4$ and K12 concentration directly determine the $d_{compact}$ and d_{porous} values, respectively, and they co-determine the entire d_{CNNC} values.

Furthermore, the composite on CE2 is depicted by HRTEM, as shown in Fig. 5. The larger-size CNF (Fig. 5 (a), (b) and (d)) reveals coarser surface than the small-size CNT (Fig. 5 (c)). These maybe mean the CNF own more defects [17,26]. To further study the defects, the composite on each CE is characterized by Raman spectrum. The tested sample is collected on the substrate and then spread uniformly. The relative intensity of I_D/I_G means the defect density (d_S) [27], indicating the disorder degree of the carbon-based materials [8,20,26], listed in Table 3. The d_S values of the

CEs except CE4 are much close, suggesting they are composed of similar component, which should be CNFs on the basis of the above results. In addition, those d_S values are bigger than that of CE4 only composed with CNTs, indicating the CNFs own more defect density. For clear exhibition, only the spectra of CE2 and CE4 are plotted, as shown in Fig. 6.

4.3. The NiSO$_4$ and K12 content effect on cell performance

4.3.1. The content effect on catalytic ability

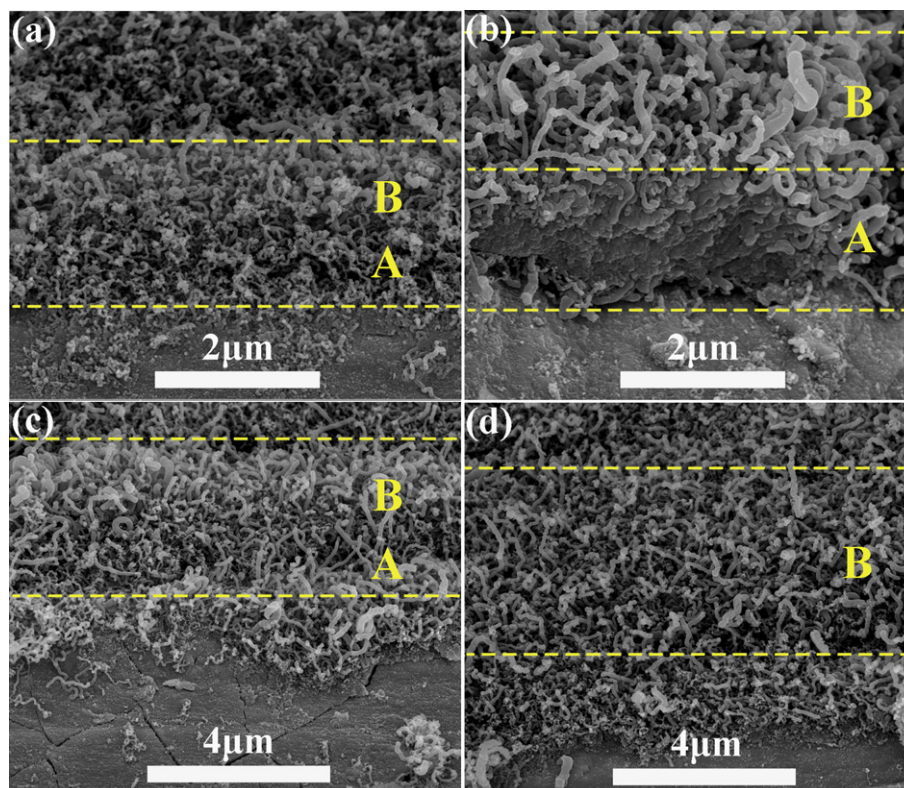In a working DSSC device with I_3^-/I_3^- redox electrolyte, a total reaction is

Fig. 4. The SEM images of CE1 (a), CE3 (b), CE5 (c) and CE6 (d) with oblique views.

$$3I^- \Leftrightarrow I_3^- + 2e^-, \qquad\qquad (1)$$

where the forward and inverted processes indicate the oxidation reaction at photoanode/electrolyte interface and reduction reaction at electrolyte/CE interface, respectively [23]. In this paper, the term of catalytic ability is defined as the total reduction ability for a CE converting I_3^- to I^-.

To study the catalytic abilities of the CEs, CV experiments are carried out with the symmetrical dummy cells. The catalytic ability can be characterized by the inverse slope of the CV plots at the zero potential [28]. A typical CV curve is composed of two sections obtained by continuously scan but with inverse direction. Generally, the two sections are overlapped at 0 V and a steeper tangent means a better catalytic ability [28]. However, as shown in Fig. 7, the two sections of every curve are just much closed to 0 V, similar to that in the literature [29]. It is likely due to the relatively bigger distance between the CEs. Even so, the catalytic ability can still be represented by the curve near 0 V. Obviously, the CE4 reveals the weakest catalytic ability by its plainest tangent. Additionally, the J_{lim} values are obtained by the extracted saturation currents. These will be used in the subsequent simulation.

Table 2
The CNNC thicknesses of the nano-carbon CEs.[a]

	Ratio[b]	$d_{compact}$ (μm)	d_{porous} (μm)	d_{CNNC} (μm)
CE1	0.016	–	–	2.0 ± 0.2
CE2	0.008	0.8 ± 0.1	2.2 ± 0.2	3.0 ± 0.3
CE3	0.004	1.5 ± 0.2	1.8 ± 0.2	3.3 ± 0.3
CE4	0	1.0 ± 0.2	0.0 ± 0.0	1.0 ± 0.2
CE5	0.016	–	–	3.5 ± 0.2
CE6	0.024	0.0 ± 0.0	4.5 ± 0.2	4.5 ± 0.2

[a] The standard error are obtained by five measurements at different locations.
[b] The concentration ratio of K12 to NiSO4.

To distinguish the catalytic ability clearly, Tafel polarization curves are measured, as shown in Fig. 8. The exchange current density J_0, obtained by the intersection of cathodic branch and equilibrium potential line [30], is extracted and listed in Table 4. A larger J_0 generally means higher ability for I_3^- reduction [30]. Here, the J_0 basically remains unchanged with the increase of $d_{compact}$ value. These indicate the compact layer cannot offer obvious catalytic effect, maybe due to it's partly (CE4) or entirely block structure (CE3), as shown in SEM images. The J_0 obviously increases with the increase of d_{porous} or d_{CNNC} value, may due to the increase of catalytic site of porous layer [31].

To confirm the catalytic ability of CEs, a controlled method of dark J–V measurement is carried out and the curves are shown in Fig. 2. With identical photoanode and electrolyte, a large dark current density generally implies high catalytic ability for CE [19,31–33]. Here, the dark current densities of all these cells show a positively relationship with their J_0 values, demonstrating the J_0 is a reasonable parameter to reflect the catalytic ability for CE.

To clearly reflect the catalytic ability, the amount of defects on each CNNC CE is estimated. On unit area of substrate, the real surface area (S_{real}) of the CNNC can be expressed as $m_{CNNC} \cdot S_{BET}$, where the S_{BET} is the BET surface area. Then, the value of $S_{real} \cdot d_S$, denoted as c_{defect}, can be used as a defect coefficient directly reflecting the catalytic ability of the CE.

The S_{BET} reveals the surface area per gram for porous materials [34,35]. Table 3 lists the measured S_{BET} values and calculated porosities for these CNNC CEs. The S_{BET} varies inversely related with the concentration ratio of K12 to NiSO4, because the CNFs own a relative small S_{BET} [36,37]. The CE3 shows the smallest S_{BET} value, which is probably due to its obvious block compact layer (Fig. 4 (b)).

As shown in Table 3, the c_{defect} basically shows a positively relationship with their J_0 value, demonstrating the J_0 value is really a reasonable parameter to reflect the catalytic ability for CE. The
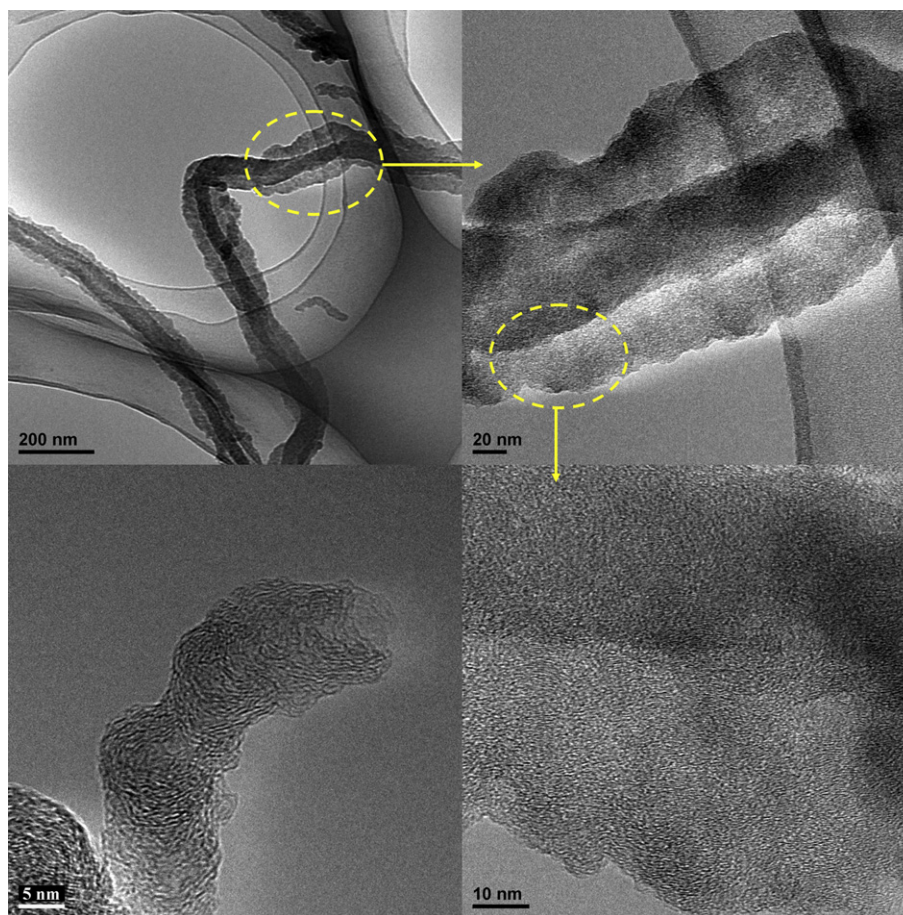
Fig. 5. The images of typical CNF and CNT observed by HRTEM.

c_{defect} varies positively with the S_{real} value, indicating the real surface area offers dominant effect to the catalytic ability than defect density. Here, the S_{real} basically increases with increasing d_{porous} value. This declares that it is the porous layer which offers the main contribution to the catalytic ability for CE. The result corresponds with that deduced above.

4.3.2. The content effect on EIS characteristics

To reveal the electrochemical characteristics, the EIS is developed and the related Nyquist and Bode-phase plots are shown in Fig. 9 (a) and (b), respectively. Referring to the equivalent circuit shown in Fig. 9 (c) and (d), the equivalent resistances fitted by Zview software are listed in Table 4. The Nyquist plots except those of CE3 and CE4 show typical spectra, each of which owns a semicircle and a beeline. They depict the interface electric response of CE/electrolyte and the electrolyte diffusion impedance, respectively. And in Fig. 9 (c), they indicate the R_{ct}-CPE_2 element and the

Z_N. The plots of CE3 and CE4 are special, each of which has an extra semicircle arising at the high frequency region. It is modeled as an added R_1-CPE_1 element shown in Fig. 9 (d). In these elements, R means charge-transfer resistance and CPE means constant phase element. The Z_N is the Warburg element.

The R_S reflects the ohm series resistance in the cell [38,39]. For these CNNC CEs, the R_S increases with increasing $d_{compact}$ or d_{porous} value, indicating a closely relationship with nano-carbon thickness.

The R_1 may come from the charge transferring in the solid–solid interface within the carbon-based materials [26,29,40]. For these CNNC CEs, only the CE3 and CE4 show obvious R_1 values, which maybe due to their clear compact layers. On the other hand, the Bode-phase plots show that the peak frequency of compact CNNC is higher than that of CNNC/electrolyte. It means the rate of electron transfer inside the former is faster than that at the later [29]. It is likely due to a high-efficiency hopping transfer mechanism between CNNCs in compact layer, besides the common tunneling

Table 3
The CNNC weight, defect density, pore parameters and defect coefficient of the CNNC CEs.[a]

	m_{CNNC} (mg cm^{-2})	d_S	S_{BET} (m^2 g^{-1})	Porosity	S_{real} (10^{-3} m^2 cm^{-2})	c_{defect} (10^{-3} m^2 cm^{-2})
CE1	0.30 ± 0.04	0.97 ± 0.01	281 ± 5	0.45 ± 0.05	85 ± 3	83 ± 3
CE2	0.34 ± 0.05	0.97 ± 0.01	285 ± 5	0.46 ± 0.04	97 ± 3	94 ± 3
CE3	0.72 ± 0.06	0.96 ± 0.01	125 ± 3	0.27 ± 0.04	90 ± 2	86 ± 2
CE4	0.23 ± 0.03	0.89 ± 0.01	295 ± 6	0.50 ± 0.04	68 ± 2	60 ± 2
CE5	0.43 ± 0.05	0.97 ± 0.01	279 ± 5	0.45 ± 0.05	120 ± 3	117 ± 3
CE6	0.50 ± 0.05	0.97 ± 0.01	257 ± 4	0.39 ± 0.08	130 ± 3	126 ± 3

[a] These parameters are all measured by five samples.

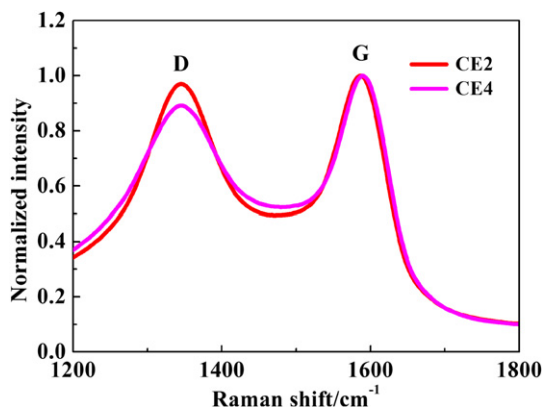**Fig. 6.** The Raman spectra of the CNNCs on CE2 and CE4. The Raman intensities are normalized to the corresponding G-band intensities.

Fig. 8. The Tafel polarization curves of CEs with the increase of $d_{compact}$ (left part) and d_{porous} values (right part). For comparison, the curve of CE0 is plotted in both parts.

conduction mechanism [41]. These indicate the compact layer promotes electron transport by acting a fast-passageway between substrate and the porous layer.

The R_{ct} is the charge-transfer resistance for electrochemical reactions, referring to the barrier through which the electron must pass across the electrode surface to the adsorbed species or from the adsorbed species to the electrode [42]. Generally, smaller R_{ct} value reflects higher catalytic ability for CE, and the R_{ct} varies inversely with J_0 [29,30]. However, this relationship is unobvious for these CNNC CEs. The measured R_{ct} value is possibly affected by the compact layer with the unique fast-passageway effect discussed above. Especially, the R_{ct} of CE4 seems to be seriously affected, because the CE is almost composed of entire compact layer. A similar effect was reported in the literature [29].

The Z_N is the diffusion impedance of the electrolyte [29]. With identical photoanode and electrolyte, the total internal impedance in DSSC device can be expressed as $R_{sum} = R_S + R_1 + R_{ct} + Z_N$ [19,39]. Here, the Z_N or R_{sum} varies positively with the d_{CNNC}. The compact layer makes R_{ct} unusual, so it may affect the measured R_{sum} value.

4.3.3. The content effect on J−V characteristics

The $J−V$ characteristics consist of the properties of V_{OC}, J_{SC}, FF and PCE. For the CNNC-based cells prepared with K12, the V_{OC} varies inversely with R_{sum}, because bigger R_{sum} value brings larger IR-drop [43]. Here, the V_{OC} values of CNNC-based cells generally exceed that of Pt-based cell (CE0). The reason maybe the formal potential of I^-/I_3^- redox reaction on carbon electrode shifted more positively than that on Pt electrode [39,43–45].
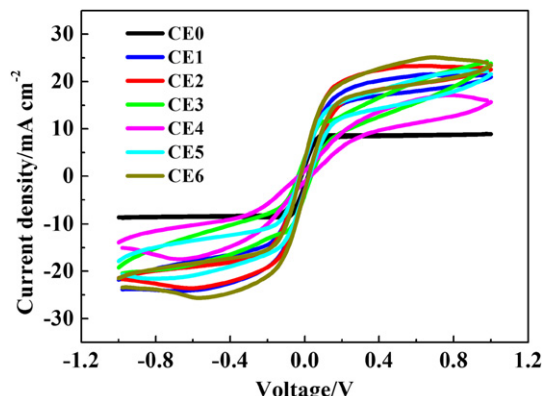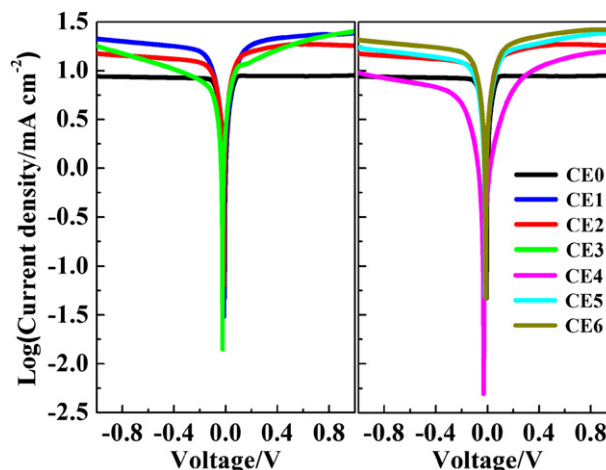
For the CNNC-based cells prepared with K12, the J_{SC} basically varies inversely with R_{sum}, because smaller internal impedance benefits charge transport in DSSC device [45]. Although higher catalytic ability (bigger J_0) offers more opportunity for reduction, the over-porous and over-thick structure here brings weak internal impedance (bigger R_{sum}), then increases the probability of charge recombination. The J_{SC} of Pt-based cell (CE0) exceeds those of CNNC-based cells. This is attributed to the mirror-like Pt layer, which increases the charge incidence efficiency by photo-reflection [8,45].

For the CNNC-based cells prepared with K12, the FF varies inversely with R_{sum}, corresponding with the literature [39,45,46]. Here, bigger J_0 is unfavorable to the FF, because it brings bigger R_{sum}, as discussed above. In addition, these FF values of CNNC-based cells generally exceed that of Pt-based cell (CE0). This may due to the unique hierarchical porous structure [34,35]. A related simulation analysis is carried out in the next section.

The cell with CE4 prepared without K12 seems unusual with the special combination of the smallest J_0 and R_{sum} values. The highest J_{SC} may due to the smallest R_{sum} value as discussed above [45]. A possible explanation of a lower V_{OC} is a localized short-circuiting between TiO$_2$ layer and CNNC layer [40]. The lowest FF is probably due to the very poor catalytic ability (the smallest J_0) [31,35]. These all ultimately due to its unique structure of CE discussed above. With a suitable combination of J_0 and R_{sum}, the cell with CE2 gives the optimal V_{OC}, J_{SC} and FF, leading to a high PCE closes to that of Pt-base cell.

4.4. The effect of CE architecture on carrier transportation

To explore the effect of CE structure on the carrier transport, a mass transport model is built for the entire DSSC device with CE0,

Fig. 7. The cyclic voltammetry plots with the symmetrical dummy cells.

Table 4
The exchange current density J_0 and the fitted equivalent resistances.[a]

CE	J_0 (mA cm^{-2})	R_S (Ω)	R_1 (Ω)	R_{ct} (Ω)	Z_N (Ω)	R_{sum} (Ω)
CE0	4.7 ± 0.1	18.3 ± 0.3	−	1.9 ± 0.2	22.7 ± 0.2	42.9 ± 0.2
CE1	4.0 ± 0.1	5.3 ± 0.3	−	14.0 ± 0.5	23.5 ± 0.2	42.8 ± 0.2
CE2	3.6 ± 0.1	9.2 ± 0.2	−	8.3 ± 0.4	22.7 ± 0.2	40.2 ± 0.2
CE3	3.6 ± 0.1	14.3 ± 0.3	1.0 ± 0.2	11.5 ± 0.2	27.1 ± 0.2	53.9 ± 0.2
CE4	0.70 ± 0.05	8.2 ± 0.3	0.4 ± 0.3	4.9 ± 0.3	20.5 ± 0.3	34.0 ± 0.4
CE5	4.4 ± 0.1	6.6 ± 0.2	−	10.5 ± 0.2	65.5 ± 0.5	82.6 ± 0.2
CE6	5.1 ± 0.2	12.0 ± 0.2	−	10.8 ± 0.3	72.1 ± 0.8	94.9 ± 0.2

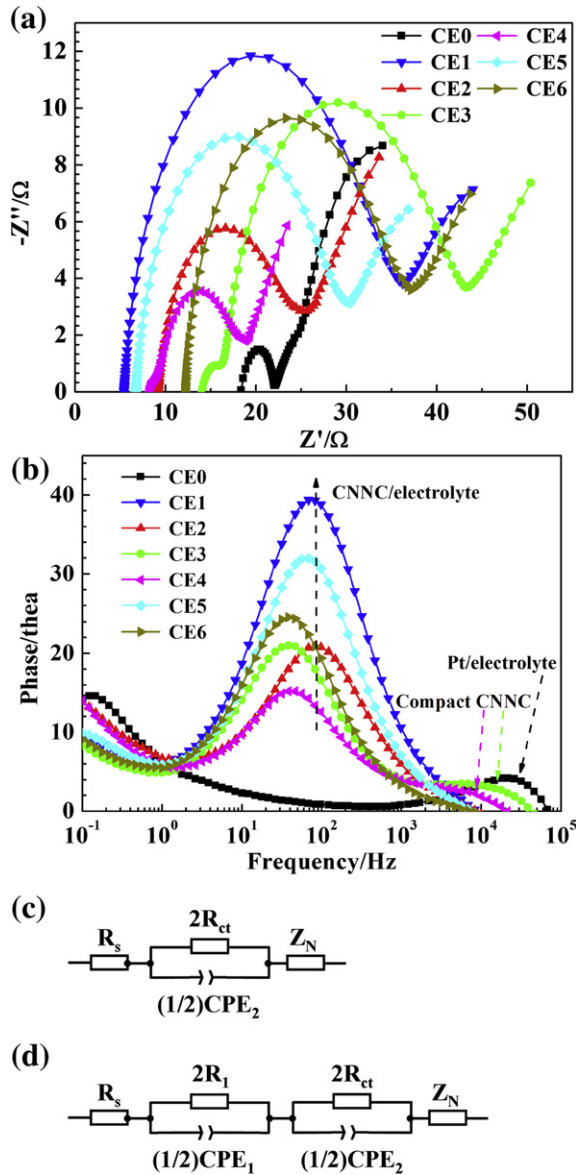[a] The results with standard error are obtained by five samples.

Fig. 9. The Nyquist (a) and Bode-phase plots (b) with the symmetrical dummy cells. (c) The equivalent circuits of the symmetrical dummy cells for CNNC CEs except CE3 and CE4. (d) The equivalent circuits for CE3 and CE4.

Table 6
Functional simulation parameters for the DSSCs with CE0, 2 and 4.

	d_{CEs} (µm)	d (µm)	J_{lim} (mA cm^{-2})	$D_{I_3^-}$ (cm^2 s^{-1})
CE0	100.0	14.0	8.62	7.45E-6
CE2	106.0	17.0	21.70	1.99E-5
CE4	102.0	15.0	13.89	1.22E-5

only in electrolyte and the p means the material porosity. The basic simulation parameters presented in Table 5 refer to the literature [23], and the functional simulation parameters shown in Table 6 are obtained according to the experiment results in this paper.

The ratio of $n_{I^-} n_{I^-,0}^{-1}$ or $n_{I_3^-} n_{I_3^-,0}^{-1}$ reflects the relative carrier concentration at the short-circuit state. It indicates the deviation level of carrier concentrations relative to their initial concentrations in electrolyte. As shown in Fig. 10, the $n_{I^-} n_{I^-,0}^{-1}$ or $n_{I_3^-} n_{I_3^-,0}^{-1}$ distribution of CE2 is the mildest, and those of CE4 are closed to those of CE0. A smooth distribution maybe means the ions are not to be accumulated near both the electrodes, and implies their fast transport. Then, the order of ion transport rate is CE2 > CE0 ≈ CE4, which is likely a suitable explanation for the order of their FF obtained in J–V characteristics. It must be noted here the transport rate is relative to the model medium, and it is different from those transport rates relative to electrolyte and photoanode, which are characterized by the D and the electron lifetime, respectively [30,47]. As a result, the transport rate in the model medium is likely co-affected by all modules in the cell, and it can be a visual parameter to reflect the integral transport property of carriers.

With identical photoanode and electrolyte, the carrier transport is just affected by the CE, *i.e.*, by J_0 and R_{sum} values. Here, they are

2 and 4. The cell approaches to a steady short-circuit state when the external load is fixed at 0.01Ω. At the short-circuit state, the concentration of I$^-$ (or I$_3^-$) in the model medium is signed as n_{I^-} (or $n_{I_3^-}$), and its initial concentrations in model medium is $n_{I^-,0}\, p$ (or $n_{I_3^-,0}\, p$). The $n_{I^-,0}$ (or $n_{I_3^-,0}$) indicates the concentration of I$^-$ (or I$_3^-$)

Table 5
Basic simulation parameters used for modeling the DSSCs.

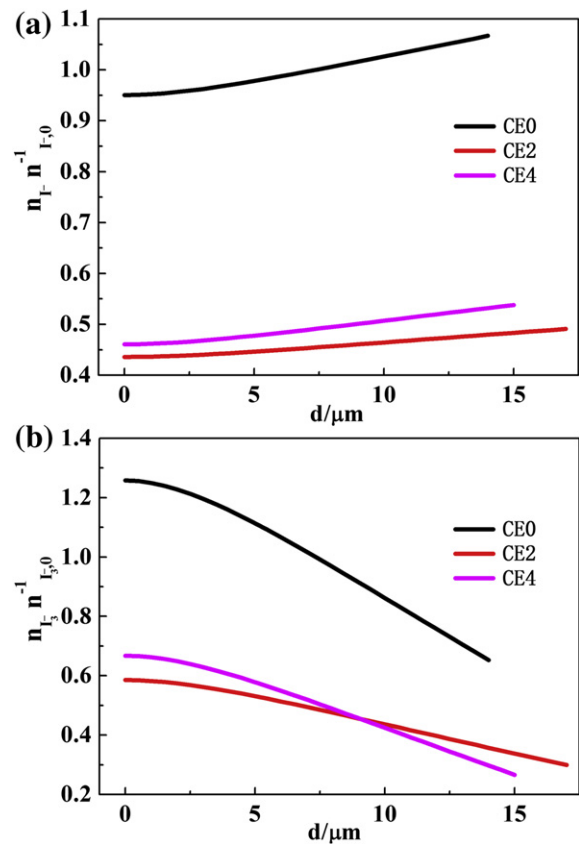| Parameter	Value
Electron relaxation rate constant	10^4 s^{-1}
Electron mobility	0.3 cm^2 V^{-1} s^{-1}
Effective mass of electron	5.6 m_e
Symmetry parameter	0.78
Effective relative dielectric constant	50
Difference of conduction band and standard electrolyte redox energy	0.93 eV
Incident spectral photon flux density	AM 1.5, 100 mW cm^{-2}
Roughness factor of TiO$_2$	1000

Fig. 10. The distributions of $n_{I^-} n_{I^-,0}^{-1}$ (a) and $n_{I_3^-} n_{I_3^-,0}^{-1}$ (b) in model medium with CE0, 2 and 4. The d indicates the location on x-axis in Fig. 1.
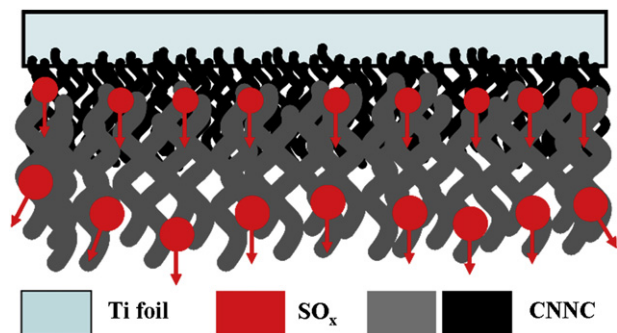
Fig. 11. The growth procedure schematic for a typical CNNC with compact and porous layers when the coated substrate is combusting in ethanol flame.

both affected by the d_{CNNC} value, *i.e.*, the architecture of CE, so the fast carrier transport is ultimately due to the suitable architecture of CE.

4.5. The composite growth procedure

Based on the forementioned characterizations and analyzes, the growth procedure for a typical CNNC with compact and porous layers is deduced. The related schematic is illustrated in Fig. 11, where the coated substrate is facing to ethanol flame with a side view. The compact layer part, porous layer part and SO_x are indicated by small black spirals, big gray spirals and red arrows, respectively.

In flame, the $NiSO_4$ and K12 are thermally decomposed. The former generates Ni nanoparticles and SO_x gases ($x = 2$, or 3), and the latter produces carbon and SO_x gases [48,49]. As inductor, the generated Ni impels the CNNC to grow. The generation and movement of SO_x make the composite hierarchical porous. The more to the surface, the more SO_x are, as shown in Fig. 11. Thus the composite in top region is more porous than that in bottom region. Moreover, the large porosity offers more opportunity for the CNNC contacting with the carbon source [17], leading large-size nanostructures forming. As a result, it is the SO_x gases, which impel the top original compact nanostructures transforming to porous nanostructures, *i.e.*, the top original compact layer transforming to the porous layer. In addition, the generated carbon decomposed from K12 as an additional carbon source further promotes the growth of CNNC. The above effect factors couple with each other during the whole growth process, and they can be adjusted by changing the contents of $NiSO_4$ and K12. With suitable contents of them, the composite with coordinating compact and porous layers for high performance DSSC counter electrode applications is fabricated.

5. Conclusion

A CNNC with unique hierarchical porous structure is fabricated as effective DSSC CE by a simple and low-cost method. The fabrication process only employs spin-coating and then combustion in ethanol flame. The $NiSO_4$ is as an inductor and the K12 is a facial pore-forming precursor. With their coordination, the generated CNNC forms unique hierarchical structure composed of compact and porous layers. The as-prepared optimized structure reveals high catalytic ability coupled with low electrical resistance. The PCE of the resulting DSSC device reaches 6.5%, which is close to 6.6% of the referenced Pt-based DSSC. Systematic characterizations are presented and a mass transport model is built. The simulation results demonstrate that the CE architecture is beneficial to carrier

transport. The fabrication strategy is simple and effective, and it provides a potential method for DSSC fabrication on a large scale.

References

[1] A. Yella, H.-W. Lee, H.N. Tsao, C. Yi, A.K. Chandiran, M.K. Nazeeruddin, E.W.-G. Diau, C.-Y. Yeh, S.M. Zakeeruddin, M. Grätzel, Science 334 (2011) 629–634.
[2] W.K. Tu, C.J. Lin, A. Chatterjee, G.H. Shiau, S.H. Chien, J. Power Sources 203 (2012) 297–301.
[3] Y.H. Jang, X.K. Xin, M. Byun, Y.J. Jang, Z.Q. Lin, D.H. Kim, Nano Lett. 12 (2012) 479–485.
[4] B. Weintraub, Y. Wei, Z.L. Wang, Angew. Chem. Int. Ed. 48 (2009) 8981–8985.
[5] Q.D. Tai, B.L. Chen, F. Guo, S. Xu, H. Hu, B. Sebo, X.Z. Zhao, ACS Nano 5 (2011) 3795–3799.
[6] N. Papageorgiou, P. Liska, A. Kay, M. Gratzel, J. Electrochem Soc. 146 (1999) 898–907.
[7] P. Dong, C.L. Pint, M. Hainey, F. Mirri, Y. Zhan, J. Zhang, M. Pasquali, R.H. Hauge, R. Verduzco, M. Jiang, H. Lin, J. Lou, ACS Appl. Mater. Interfaces 3 (2011) 3157–3161.
[8] W.J. Lee, E. Ramasamy, D.Y. Lee, J.S. Song, ACS Appl. Mater. Interfaces 1 (2009) 1145–1149.
[9] P. Joshi, L. Zhang, Q. Chen, D. Galipeau, H. Fong, Q. Qiao, ACS Appl. Mater. Interfaces 2 (2010) 3572–3577.
[10] J.G. Nam, Y.J. Park, B.S. Kim, J.S. Lee, Script. Mater. 62 (2010) 148–150.
[11] W.C. Huang, X.L. Zhang, F.Z. Huang, Z.P. Zhang, J.J. He, Y.B. Cheng, J. Nanopart. Res. 14 (2012).
[12] G.T. Yue, J.H. Wu, Y.M. Xiao, J.M. Lin, M.L. Huang, Electrochim. Acta 67 (2012) 113–118.
[13] Z. Huang, X. Liu, K. Li, D. Li, Y. Luo, H. Li, W. Song, L. Chen, Q. Meng, Electrochem Commun. 9 (2007) 596–598.
[14] C.-K. Hsieh, M.-C. Tsai, C.-Y. Su, S.-Y. Wei, M.-Y. Yen, C.-C.M. Ma, F.-R. Chen, C.-H. Tsai, Chem. Commun. 47 (2011) 11528–11530.
[15] C.-K. Hsieh, M.-C. Tsai, M.-Y. Yen, C.-Y. Su, K.-F. Chen, C.-C.M. Ma, F.-R. Chen, C.-H. Tsai, Phys. Chem. Chem. Phys. 14 (2012) 4058–4061.
[16] N. Liu, G. Fang, X. Yang, W. Zeng, C. Li, M. Wang, J. Li, X. Zhao, Diam. Relat. Mater. 18 (2009) 1375–1380.
[17] X. Qi, J. Zhang, C.X. Pan, J. Mater. Sci. Technol. 24 (2008) 603–607.
[18] Y.L. Liu, Q. Fu, C.X. Pan, Carbon 43 (2005) 2264–2271.
[19] E. Ramasamy, W.J. Lee, D.Y. Lee, J.S. Song, Electrochem Commun. 10 (2008) 1087–1089.
[20] X.G. Mei, S.J. Cho, B.H. Fan, J.Y. Ouyang, Nanotechnology 21 (2010) 395202.
[21] S. Ito, T.N. Murakami, P. Comte, P. Liska, C. Grazel, M.K. Nazeeruddin, M. Grazel, Thin Solid Films 516 (2008) 4613–4619.
[22] J.N. Hart, D. Menzies, Y.B. Cheng, G.P. Simon, L. Spiccia, Compt. Rend. Chim. 9 (2006) 622–626.
[23] J. Ferber, R. Stangl, J. Luther, Sol. Energy Mater. Sol. Cells 53 (1998) 29–54.
[24] K. Miettunen, J. Halme, A.-M. Visuri, P. Lund, J. Phys. Chem. C 115 (2011) 7019–7031.
[25] J. Halme, P. Vahermaa, K. Miettunen, P. Lund, Adv. Energy Mater. 22 (2010) E210–E234.
[26] S.H. Seo, S.Y. Kim, B.-K. Koo, S.-I. Cha, D.Y. Lee, Langmuir 26 (2010) 10341–10346.
[27] H.Y. Wang, F.M. Wang, Y.Y. Wang, C.C. Wan, B.J. Hwang, R. Santhanam, J. Rick, J. Phys. Chem. C 115 (2011) 8439–8446.
[28] L. Kavan, J.-H. Yum, M. Grätzel, Nano Lett. 11 (2011) 5501–5506.
[29] S. Huang, H. Sun, X. Huang, Q. Zhang, D. Li, Y. Luo, Q. Meng, Nanoscale Res. Lett. 7 (2012) 222.
[30] M. Wu, X. Lin, Y. Wang, L. Wang, W. Guo, D. Qi, X. Peng, A. Hagfeldt, M. Grätzel, T. Ma, J. Am. Chem. Soc. 134 (2012) 3419–3428.
[31] G. Veerappan, K. Bojan, S.-W. Rhee, Renew. Energy 41 (2012) 383–388.
[32] S. Ito, P. Liska, P. Comte, R. Charvet, P. Pechy, U. Bach, L. Schmidt-Mende, S.M. Zakeeruddin, A. Kay, M.K. Nazeeruddin, M. Gratzel, Chem. Commun. (2005) 4351–4353.
[33] G. Veerappan, K. Bojan, S.-W. Rhee, ACS Appl. Mater. Interfaces 3 (2011) 857–862.
[34] S.Q. Fan, B. Fang, J.H. Kim, B. Jeong, C. Kim, J.S. Yu, J. Ko, Langmuir 26 (2010) 13644–13649.
[35] B. Fang, S.-Q. Fan, J.H. Kim, M.-S. Kim, M. Kim, N.K. Chaudhari, J. Ko, J.-S. Yu, Langmuir 26 (2010) 11238–11243.
[36] S.L. Knupp, W. Li, O. Paschos, T.M. Murray, J. Snyder, P. Haldar, Carbon 46 (2008) 1276–1284.
[37] P. Serp, M. Corrias, P. Kalck, Appl. Catal. A Gen. 253 (2003) 337–358.

[38] K. Fan, T. Peng, B. Chai, J. Chen, K. Dai, Electrochim. Acta 55 (2010) 5239–5244.
[39] Q. Wang, S. Ito, M. Gratzel, F. Fabregat-Santiago, I. Mora-Sero, J. Bisquert, T. Bessho, H. Imai, J. Phys. Chem. B 110 (2006) 25210—25221.
[40] T.N. Murakami, S. Ito, Q. Wang, M.K. Nazeeruddin, T. Bessho, I. Cesar, P. Liska, R. Humphry-Baker, P. Comte, P. Pechy, M. Gratzel, J. Electrochem Soc. 153 (2006) A2255—A2261.
[41] T. Chen, Z. Cai, Z. Yang, L. Li, X. Sun, T. Huang, A. Yu, H.G. Kia, H. Peng, Adv. Mater. 23 (2011) 4620—4625.
[42] L. Kavan, J.H. Yum, M. Gratzel, ACS Nano 5 (2011) 165—172.
[43] K. Imoto, K. Takahashi, T. Yamaguchi, T. Komura, J.-i. Nakamura, K. Murata, Sol. Energy Mater. Sol. Cells 79 (2003) 459—469.
[44] E. Ramasamy, W.J. Lee, D.Y. Lee, J.S. Song, Appl. Phys. Lett. 90 (2007) 173103.
[45] R. Jia, J. Chen, J. Zhao, J. Zheng, C. Song, L. Li, Z. Zhu, J. Mater. Chem. 20 (2010) 10829—10834.
[46] R.S. Mane, W.-J. Lee, C.D. Lokhande, B.W. Cho, S.-H. Han, Curr. Appl. Phys. 8 (2008) 549—553.
[47] N. Huang, Y. Liu, T. Peng, X. Sun, B. Sebo, Q. Tai, H. Hu, B. Chen, S.-s. Guo, X. Zhao, J. Power Sources 204 (2012) 257—264.
[48] J. Straszko, J. Możejko, M. Olszak-Humienik, J. Therm. Anal. Calorim. 45 (1995) 1109—1116.
[49] J.M. Patterson, Z. Kortylewicz, W.T. Smith, J. Agric. Food Chem. 32 (1984) 782—784.